J. Fluid Mech. (2008), *vol.* 599, *pp.* 341–362. © 2008 Cambridge University Press
doi:10.1017/S0022112008000190 Printed in the United Kingdom

Onset of motion of a three-dimensional droplet on a wall in shear flow at moderate Reynolds numbers

HANG DING AND PETER D. M. SPELT
Department of Chemical Engineering, Imperial College London, SW7 2AZ, UK

(Received 16 July 2007 and in revised form 4 December 2007)

We investigate the critical conditions for the onset of motion of a three-dimensional droplet on a wall in shear flows at moderate Reynolds number. A diffuse-interface method is used for this purpose, which also circumvents the stress singularity at the moving contact line, and the method allows for a density and viscosity contrast between the fluids. Contact-angle hysteresis is represented by the prescription of a receding contact angle θ_R and an advancing contact angle value θ_A. Critical conditions are determined by tracking the motion and deformation of a droplet (initially a spherical cap with a uniform contact angle θ_0). At sufficiently low values of a Weber number, *We* (based on the applied shear rate and the drop volume), the drop deforms and translates for some time, but subsequently reaches a stationary position and attains a steady-state shape. At sufficiently large values of *We* no such steady state is found. We present results for the critical value of *We* as a function of Reynolds number *Re* for cases with the initial value of the contact angle $\theta_0 = \theta_R$ as well as for $\theta_0 = \theta_A$. A scaling argument based on a force balance on the drop is shown to represent the results very accurately. Results are also presented for the static shape, transient motion and flow structure at criticality. It is shown that at low *Re* our results agree (with some qualifications) with those of Dimitrakopoulos & Higdon (1998, *J. Fluid Mech.* vol. 377, p. 189). Overall, the results indicate that the critical value of *We* is affected significantly by inertial effects at moderate Reynolds numbers, whereas the steady shape of droplets still shows some resemblance to that obtained previously for creeping flow conditions. The paper concludes with an investigation into the complex structure of a steady wake behind the droplet and the occurrence of a stagnation point at the upstream side of the droplet.

1. Introduction

Shear flow past a three-dimensional droplet on a wall serves as a model problem for a variety of flows that are of practical interest. Well-studied are, for example, water droplets detached from porous surfaces in fuel cells (Theodorakakos *et al.* 2006), oil-drop removal from steel surfaces (Thoreau *et al.* 2006), and the rate of condensation (or deposition) of droplets on a pipe wall; also, it may be considered to be a model for the determination of the yield criteria of cells adhering to biological surfaces, albeit that there an added complexity is the presence of adhesive forces between interfaces (e.g. Cao *et al.* 1998; Hodges & Jensen 2002) that is beyond the scope of this paper. It remains unclear under what circumstances droplets remain on the wall, or even at a fixed location on the wall. Properties of the surface of the solid substrate may be expected to play an important role in this process. In particular, chemical inhomogeneities or wall roughness may lead to contact-angle hysteresis (de Gennes 1985; Joanny & Robbins 1990); for a recent approach relating hysteresis to properties of heterogeneities, see Thiele & Knobloch (2006). As has been demonstrated experimentally, hysteresis can lead to critical conditions below which droplets on inclined surfaces can remain pinned (Quéré, Azzopardi & Delattre 1998; Ha, Park & Lee 2005; Berejnov & Thorne 2007). In the present context, contact-angle hysteresis may result in a minimum shear rate below which droplets are expected to yield, possibly leading to a continously moving, a partially entrained, or a moving partially entrained drop. Some of these regimes have been observed experimentally (albeit under creeping-flow conditions), see Mahé *et al.* (1988) and Thoreau *et al.* (2006). Of direct practical interest is the ability to predict the corresponding yield criterion.

We focus here on the transition from a stationary drop to a continuously moving drop. We investigate this problem for a three-dimensional droplet, accounting for fluid inertia; the three-dimensional creeping-flow problem and, to some extent, the two-dimensional problem with inertia have been the subject of previous work, which is summarized briefly below. Unlike in previous work on the three-dimensional problem, the numerical method used here allows the contact line to move, thereby providing an additional opportunity to revisit the creeping-flow problem.

In previous work on the creeeping-flow problem, Mahé *et al.* (1988) showed that experimental data for the yield criterion could be represented by a critical value of a capillary number. Dimitrakopoulos & Higdon (1998) solved an optimization problem based on the steady-state form of the governing equations to determine the optimum drop shape that leads to the maximum shear rate for which the drop can adhere to the wall. This work followed earlier investigations wherein the contact line was fixed (Li & Pozrikidis 1996). Dimitrakopoulos & Higdon (1998) concluded that fundamentally different optimum shapes result when constraints are imposed on the drop shape, leading to different critical shear rates. The authors put forward a hypothesis of how the various shapes could be recovered experimentally. More recently, Dimitrakopoulos (2007) was able to determine which part of a fixed circular contact line would start to move first for a large range of cases under creeping-flow conditions. The numerical method used in the present paper, besides enabling us to investigate inertial effects, allows motion of the contact line, and hence the possibility that drops, after some motion, eventually come to a halt. We can therefore compare directly the resulting steady shape at critical conditions with those obtained by Dimitrakopoulos & Higdon (1998).

Current insight into inertial effects in the criteria for the onset of motion of three-dimensional drops is limited to various studies of two-dimensional droplets. Durbin (1988) used inviscid theory to determine the yield criterion for very slender two-dimensional drops, such that the contact angle values are small, but in the presence of free-streamline separation from the drop. More recently, one of us (Spelt 2006) used numerical simulations to determine inertial effects on the yield criterion for the direct transition from a stationary two-dimensional droplet to an approach to partial entrainment. The critical value of a Weber number $We = \rho\dot{\gamma}^2a^3/\sigma$ was found to approach a constant value when the value of a Reynolds number $Re = \rho\dot{\gamma}a^2/\mu$ was increased, the creeping-flow regime corresponding to a critical value of the capillary number $Ca = We/Re$. Here, ρ and μ are the density and viscosity of the surrounding fluid, respectively, a is an effective drop radius, $\dot{\gamma}$ is the imposed shear rate, and σ is the surface tension coefficient. The results were sensitive to the ratios of the densities and viscosities of the two fluids. A second part of that work focused on two-dimensional drops that move on perfectly clean flat surfaces; this was also the subject of a study by Zhang, Miksis & Bankoff (2006), who identified various flow

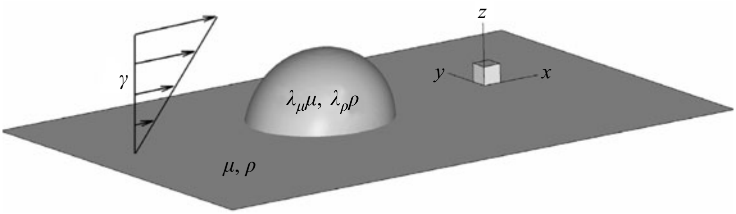

FIGURE 1. A droplet rests on a solid substrate in a shear flow.

regimes in terms of *We* and *Re*. The transition from a static to a moving drop was not considered in those studies.

We investigate here numerically the critical condition for the onset of motion, the drop shape at criticality, and the wake structure, for three-dimensional droplets at moderate values of *Re*. Various methods are currently available for the numerical simulation of driven droplets, including a slip formulation (e.g. Spelt 2006), lattice Boltzmann (e.g. Hyväluoma *et al.* 2007), and dissipative particle dynamics (e.g. Jones *et al.* 1999). Here, building on previous experience (Ding & Spelt 2007*a*), we use a diffuse-interface method, which allows the contact line to move before coming to a halt. In this method, the finite thickness of the interface alleviates the stress singularity at a moving contact line (Seppecher 1996; Jacqmin 2000). Previous work on droplet spreading (Ding & Spelt 2007*a*) has shown that the results obtained from this method are similar to those from a sharp-interface method where slip is introduced, the effective slip length being approximately proportional to the interface thickness; a comparison with lubrication theory was also provided. There are two limitations in this numerical study. First, the interfacial region is only resolved within the limits of the computational resources available, leading to an effective value of the slip length that is much larger than those inferred from experimental data (Marsh, Garoff & Dussan V. 1993). However, the thickness of the interface can be varied to some extent, and some evidence of the effect of the effective slip length on the results is provided below. A second limitation of this study is that only microscopic surface inhomogeneities are considered. Instead of being modelled explicitly, as in Nikolayev (2005) and Hyväluoma *et al.* (2007), they are modelled by a window of contact-angle hysteresis. Preliminary results by Spelt (2006) wherein such an approach was attempted show the complexity of the results. Instead, in the present paper, the presence of surface inhomogeneities is modelled by prescribing a window of contact-angle hysteresis, i.e. a range of values of the contact angle wherein the contact line remains stationary. This will provide a basis for more complex systems such as those wherein inhomogeneities are represented explicitly. This approach will also facilitate a direct comparison with the earlier work in this area (cf. Dimitrakopoulos & Higdon 1998). Further details on the problem statement and numerical method are given in the next section.

2. Problem statement and numerical method

2.1. *Problem statement*

A problem sketch is provided in figure 1. Both the droplet and the surrounding fluid are incompressible, viscous and immiscible. The droplet viscosity and density are denoted by μ and ρ, respectively. The ratio of the density (viscosity) of the droplet to that of the surrounding fluid is denoted by λ_ρ (λ_μ). The shear rate $\dot{\gamma} = U/H$ is maintained by moving the upper boundary of the domain, at the height of H, with a constant speed U. We have made the equations of motion dimensionless using the inverse of the shear rate $1/\dot{\gamma}$ and the drop size $a=(3V/(4\pi))^{1/3}$ (where V is the drop volume) as the characteristic time and length scale, respectively. The droplet has constant surface tension coefficent and the effects of gravity are considered to be negligible. Note that for illustrative purposes all the shapes of the droplet and contact lines presented in the following sections have been rescaled by $R=2^{1/3}a$, which corresponds to the radius of the contact line with $\theta=90°$ everywhere.

In all calculations reported here, half of the drop has been simulated. The imposed boundary conditions are the following. At the inlet boundary, $\partial u/\partial x=0$ and $v=w=0$; at the outlet boundary, $\partial \boldsymbol{u}/\partial x=0$, where (u, v, w) are the velocity components in the (x, y, z) directions (see figure 1). At both side boundaries (normal to the y-direction), symmetry boundary conditions are used (with $v=0$). No-slip boundary conditions are enforced at the upper and lower boundaries. The (dimensionless) size of the computational domain is $12.6\times 4.2\times 4.2$, wherein the height and width of the domain are chosen in such a way that the effect of the upper solid wall is negligible (this has been confirmed by numerical experiments). At the start of the simulations, the droplet rests on the solid substrate at $x=3.78$. The initial velocity field outside the drop corresponds to the imposed shear flow, whereas inside the drop it is set to zero. This may serve as an approximation of experimental conditions wherein a droplet would be placed rapidly on the wall, either by injection through the wall or by deposition. Ideally, the initial velocity field would be zero everywhere in the domain, and the upper wall would be set in motion impulsively, as in our previous work (Spelt 2006). Such computations proved to take an excessive time to run before a drop would reach a stationary position. We have conducted numerical experiments at $Re=0.684$ using a zero initial velocity field, and the results were indistinguishable from those using the present initial conditions.

2.2. *Diffuse-interface model and boundary conditions*

We use here a diffuse-interface method to model the time evolution of the interfacial shape in the presence of a moving contact line (Jacqmin 2000; Ding & Spelt 2007*b*). The diffuse-interface method originates from the investigation of critical phenomena (Hohenberg & Halperin 1977) (for a more recent review of diffuse-interface methods, and the so-called *Model H* used here, see Anderson, McFadden & Wheeler 1998). In this method, a scalar order parameter (here the volume fraction of one of the fluids, denoted by C) is employed to describe the interface, and it varies relatively smoothly across the interface (which is of finite thickness) compared to sharp-interface models. The scalar field of C is advected by the incompressible velocity field $\boldsymbol{u}$, whilst being diffused due to spatial inhomogeneities of the fluids. This process is modelled by the convective Cahn–Hilliard (CH) equation

$$\frac{\partial C}{\partial t}+\nabla\cdot(\boldsymbol{u}C)=M\nabla^2\psi, \tag{2.1}$$

where M is the mobility, ψ $(=\phi'(C)-\epsilon^2\nabla^2 C)$ the chemical potential; ϵ represents a measure of the thickness of the diffuse interface ($\epsilon \ll a$ is required for accurate simulations); $\phi=C^2(1-C)^2/4$ is the bulk energy density. The Cahn–Hilliard equation is combined with a single set of Navier–Stokes equations for variable-density and-viscosity fluids (Jacqmin 1999; Ding, Spelt & Shu 2007). The jump in viscosity and density across the interface in the sharp limit is smoothed using a linear approximation $\mu(C)=[C+(1-C)\lambda_\mu]\mu$ and $\rho(C)=[C+(1-C)\lambda_\rho]\rho$. The surface tension force per unit volume is represented in the momentum equation by an additional term $6\sqrt{2}\epsilon^{-1}\sigma\psi\nabla C$. Results of various test cases for fluids of different density can be found in Ding *et al.* (2007) (as well as in Ding & Spelt 2007*a*). In the present paper essentially the same code is used. It is a finite volume method on a marker-and-cell (MAC) mesh: velocity components are defined at the cell faces and scalar variables such as pressure and volume fraction are defined at the cell centres. Owing to the advecting nature of the convective CH equation, a fifth-order weighted essentially non-oscillatory (WENO) scheme (Liu, Osher & Chan 1994) is employed in the discretization of the advection term (the second term on the left-hand side of (2.1)) using the local flow velocity as the upwinding direction. As a result, under- and overshoots in the volume fraction profile across the diffuse interface are significantly surpressed; also, tests show that mass is globally well conserved (Ding *et al.* 2007).

The wetting condition serves as a boundary condition for the diffuse interface at the solid substrate, and is enforced by using a so-called *geometric formulation* (Ding & Spelt 2007*b*), which results in a diffuse interface at the contact line with a slope value that is consistent with the prescibed contact angle. We have shown recently that, to a reasonable approximation, the effective slip length arising from the diffuse interface (with a no-slip condition) is approximately twice the thickness of the diffuse interface (Ding & Spelt 2007*a*). A window of contact-angle hysteresis

$$\left.\begin{array}{rr} \theta=\theta_A & \text{if } U_{cl}>0, \\ \theta=\theta_R & \text{if } U_{cl}<0, \\ \theta_R<\theta<\theta_A & \text{if } U_{cl}=0 \end{array}\right\} \tag{2.2}$$

(cf. Hocking 1981), where U_{cl} denotes the velocity of the contact line, is represented in the diffuse-interface method as follows. At each time step, a first approximation of the local contact angle is obtained as in Ding & Spelt (2007*b*). If this value is outside the hysteresis window, either the advancing or receding contact angle value is prescribed instead; this is achieved by setting the appropriate value of C at a layer of ghost cells in the wall (cf. Ding *et al.* 2007). If the first approximation of the local contact angle is between θ_R and θ_A, the corresponding value of C in the ghost cell remains unchanged. Having then set C in the entire layer of ghost cells, the process is repeated as part of the iterative procedure conducted at each time step (the CH equation is solved in a semi-implicit manner, as explained in Ding *et al.* 2007). This implementation of the condition (2.2) is similar to that proposed by Spelt (2005) for a level-set method, and Dupont, Legendre & Morgante (2007) for a VOF method. Results obtained with the code for $\theta_A=\theta_R$ have been compared with those from a level-set method in Ding & Spelt (2007*a*); comparisons with creeping-flow theory for flows with contact-angle hysteresis are provided in § 3 below.

2.3. *Criteria for identifying critical conditions for the onset of droplet motion*

In all simulations conducted here wherein a stationary droplet was eventually obtained, the drop would first deform, then start to move, and finally come to a stop; and for those beyond criticality the droplet would continue to move. The critical value of *We* (at a given value of *Re* and window of contact-angle hysteresis) in our work is therefore based on whether the droplet eventually stops moving, not whether a droplet with e.g. a circular contact line will start to move (this has been studied recently by Dimitrakopoulos 2007). This was determined as follows.

When approaching critical conditions from below (i.e. from lower, stable values of *We*), it was found that either the contact angle at the upstream end (denoted here by θ_U) approached the prescribed value of the receding angle, or the contact

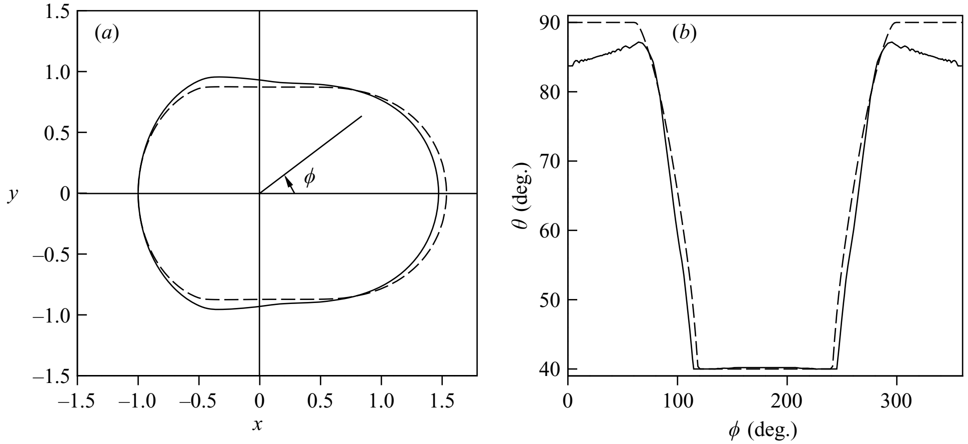

FIGURE 2. Comparison between results for cases that are at and above criticality according to criterion (2.3): $We = 1.01$ (at criticality; solid line) and 1.05 (beyond criticality; dashed line) for $\theta_0 = 90°$, $\theta_A = 90°$, $\theta_R = 40°$ and $Re = 13.7$. The lines represent (*a*) the contact line (the drops have been shifted such that their upstream ends coincide) and (*b*) the contact angle distribution, where the angle ϕ is defined in (*a*).

angle at the downstream end of the droplet (denoted here by θ_D) approached the advancing contact angle value. It proved convenient to adopt the following procedure to determine the critical conditions. At a given value of *Re*, the value of *We* would be increased until the following criterion was met after a maximum simulation time of T_c:

$$\max\{\theta_U - \theta_R, \theta_A - \theta_D\} \leqslant \xi. \tag{2.3}$$

Then, a lower value would be chosen for *We* until this criteri met. Here, ξ is a small positive constant, which controls the undershoot in the critical value of the Weber number. In this study, we use $T_c = 60$, $\xi = 3°$ for $Re \leqslant 13.7$ and $\xi = 8°$ for $Re > 13.7$ unless specified otherwise.

As an example of the performance of the above criterion in determining the critical condition, at $Re = 13.7$, the resulting critical Weber number is $We_c = 1.01$. In figure 2, a comparison is shown of the contact line shape and contact angle distributions for $We = 1.01$ and 1.05. It was found that at $We = 1.05$, the droplet eventually moves at a (dimensionless) speed of 0.032.

2.4. *Cases considered*

A series of computations has been conducted on a MAC mesh of $300 \times 100 \times 100$ cells to determine the critical conditions for a range of values of *Re*, as well as the flow structure for flows of fluids that are not density- and viscosity-matched. In order to study the generic problem of the displacement of a drop by shear flow, gravity has not been taken into account in the simulations reported here. Hence a Bond number $\rho(\lambda_\rho - 1)ga^2/\sigma$ is assumed to be small (the effect of gravity has been studied for the creeping-flow regime by Dimitrakopoulos & Higdon 1999). A moderate contact-angle hysteresis window of $\theta_A = \pi/2$ and $\theta_R = 2\pi/9$ is used in most cases. The initial configuration is specified by the contact angle θ_0 of the initial spherical-cap shape of the drop ($\theta_R \leqslant \theta_0 \leqslant \theta_A$). Three cases will be referred to in the following discussion: Case A ($\theta_A = 90°$, $\theta_R = 40°$ and $\theta_0 = 40°$); Case B ($\theta_A = 90°$, $\theta_R = 50°$ and $\theta_0 = 90°$) and Case C ($\theta_A = 90°$, $\theta_R = 40°$ and $\theta_0 = 90°$).

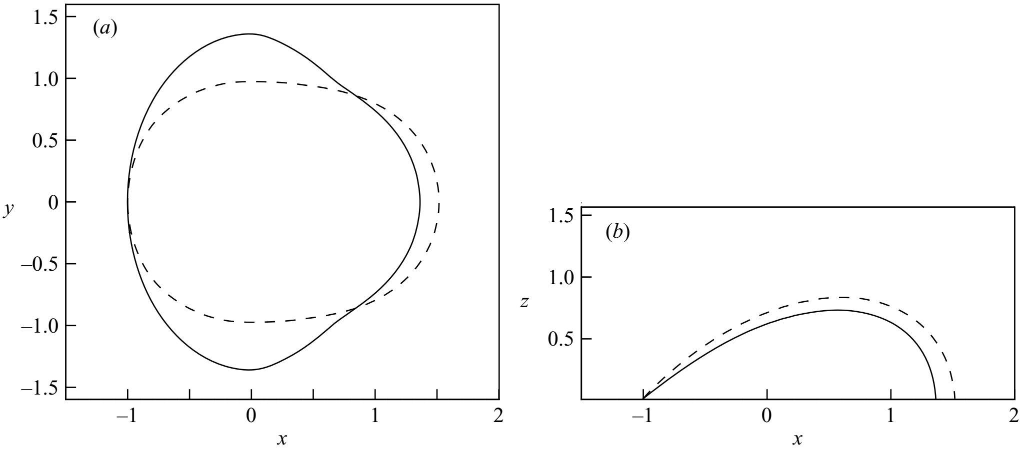

FIGURE 3. Shapes of the contact line and cross-section at $Re = 0.684$ at criticality. (*a*) Contact line, (*b*) cross-section at the symmetry plane. Solid line represents Case A at $We_c = 0.0866$, dashed line represents Case B at $We_c = 0.0554$. The drops have been shifted such that their upstream ends coincide for clarity.

3. Results

We investigate here critical conditions for the onset of motion of drops. In most cases, the fluids are density- and viscosity-matched; the effect of these latter ratios is investigated in § 3.5). Therefore, the values of λ_μ and λ_ρ are only stated when they are not equal to unity.

3.1. *Comparison with previous work: constrained vs. unconstrained spreading*

We compare here results for low values of *Re* with those obtained by Dimitrakopoulos & Higdon (1998), who used a completely different method to solve the equations of motion and to determinate critical conditions. This test is also used here to investigate under what circumstances the optimum shapes determined by Dimitrakopoulos & Higdon (1998) can be obtained (their results having been obtained from solving the equations of motion at steady state). They presented two different sets of solutions for a given window of contact-angle hysteresis. In one set, no constraint on the contact line was imposed. In the second, the contact line was not allowed to extend further in the y-direction than the extent of a circular cap of the same volume with a uniform contact angle equal to θ_A. Dimitrakopoulos & Higdon (1998) hypothesized that the unconstrained solutions could be observed in experiment by arranging for $\theta_0 = \theta_R$, whereas arranging for $\theta_0 = \theta_A$ would lead to y-constrained solutions. For these reasons, we consider Cases A and B for the comparison, corresponding to what one would expect on the basis of this previous work to be an unconstrained and a y-constrained case, respectively.

The contact line and the interfacial shape of the cross-section of the droplet at critical conditions are shown in figure 3, which should be compared with figures 4 and 6 in Dimitrakopoulos & Higdon (1998); quantitative details of the comparison are listed in table 1 (no data are available from Dimitrakopoulos & Higdon (1998) for Case C). The critical values of the capillary number are seen to be in reasonable agreement. The dimensions of the drop at criticality are also in good agreement, but with the notable exception of the width of the contact line in Case A. To investigate this single discrepancy briefly in more detail, we first note that the drop width obtained

Case	Ca_c	Length	Width	Height
A	0.127 (0.120)	2.36 (2.23)	2.72 (3.15)	0.73 (0.75)
B	0.081 (0.080)	2.51 (2.49)	1.95 (2.00)	0.84 (0.86)

TABLE 1. Comparision of the capillary number and the dimensions of the droplet at criticality for $Re = 0.684$ with values inferred from Dimitrakopoulos & Higdon (1998) for creeping flows (given in parentheses).

by Dimitrakopoulos & Higdon (1998) for Case A is larger than the diameter of the initial circular contact line (which is equal to 3.04). This could have been achieved in the present simulations if the contact line had spread. In order for that to happen, the shear flow would have had to bend the interface in the y-direction, which evidently has not occurred. A careful inspection of the contact angle distribution along the contact line (e.g. figure 10 below) reveals why spreading has been inhibited in the lateral direction in Case A. In both our solutions and those from Dimitrakopoulos & Higdon (1998), the lateral edge of the contact line at criticality in Case A is located at the place where the transition of the contact angle from the receding angle to the window of hysteresis occurs. This is also the case during the evolution of the contact line (see e.g. figure 5). Therefore, this part of the contact line is only able to 'recede', rather than 'spread', and as a result the width of the droplet does not exceed the initial radius of the contact line.

Overall, therefore, the present simulations confirm that, at low values of Re, the unconstrained and the y-constrained solution presented by Dimitrakopoulos & Higdon (1998) can be recovered as outlined above, but that an initial shape other than a spherical cap would be required to get very close agreement with the unconstrained results of Dimitrakopoulos & Higdon (1998).

3.2. *Manner of approach to a stationary position of drops at moderate Re*

Before proceeding with presenting results on critical conditions at moderate values of Re, we investigate here briefly the extent to which and the manner in which droplets move downstream in their entirety as they approach a stationary position. In order to have a consistent surface condition of the solid substrate, we consider here Cases A and C, which have the same window of contact-angle hysteresis but correspond to different initial configurations.

The temporal droplet motion is illustrated in figures 4 and 5 for Cases A and C at $Re = 0.684$ and 74.1, by showing snapshots of the shape of the contact line and cross-section of the droplet at various times. It can be seen from these results that, depending on the initial configuration, the motion of the contact line starts either at the upstream side of the droplet (e.g. Case A) or the downstream side (e.g. Case C).

The net displacement of the entire droplet is seen to be much more significant (especially in Case C) at relatively large values of Re than in the creeping-flow regime, and the motion is non-monotonic. Closer inspection of the high-Re results in figure 4 shows that the downstream side of the drop rocks back and forth. From these data we have attempted to determine the value of the maximum angle that the interface makes with the horizontal in the contact-line region, which serves as an estimate of a macro-scale contact angle (cf. Ding & Spelt 2007*a*). Although a very fine grid would be required to give an accurate signal of this angle as a function of time, the results available here (which are therefore not shown) do suggest that

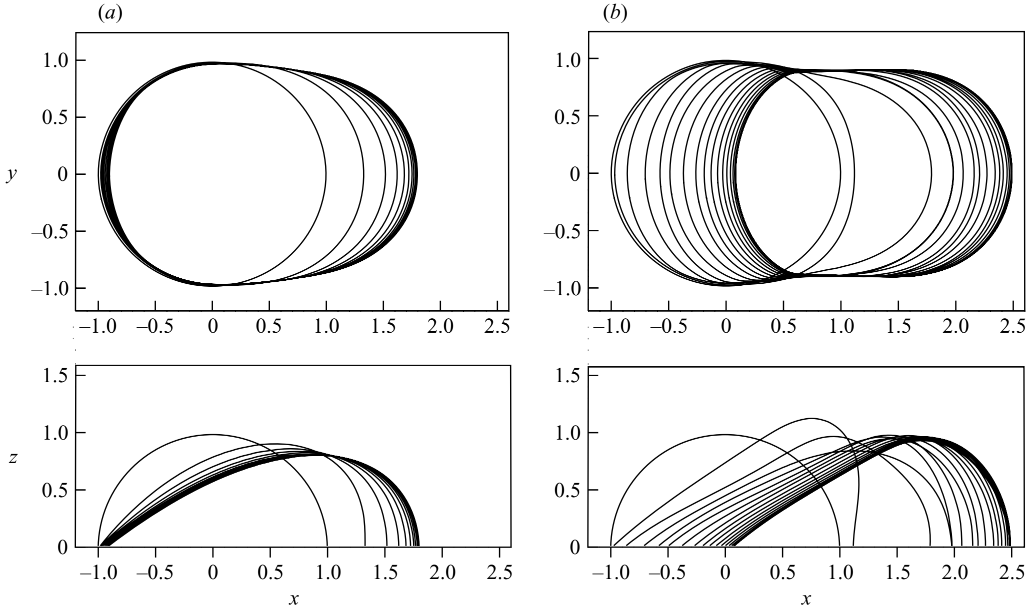

FIGURE 4. Snapshots of the droplet at a time interval of 2 for Case C at criticality. (*a*), $Re = 0.684$ and $We_c = 0.067$; (*b*) $Re = 74.1$ and $We_c = 3.01$. Contact lines (upper), cross-section (lower).

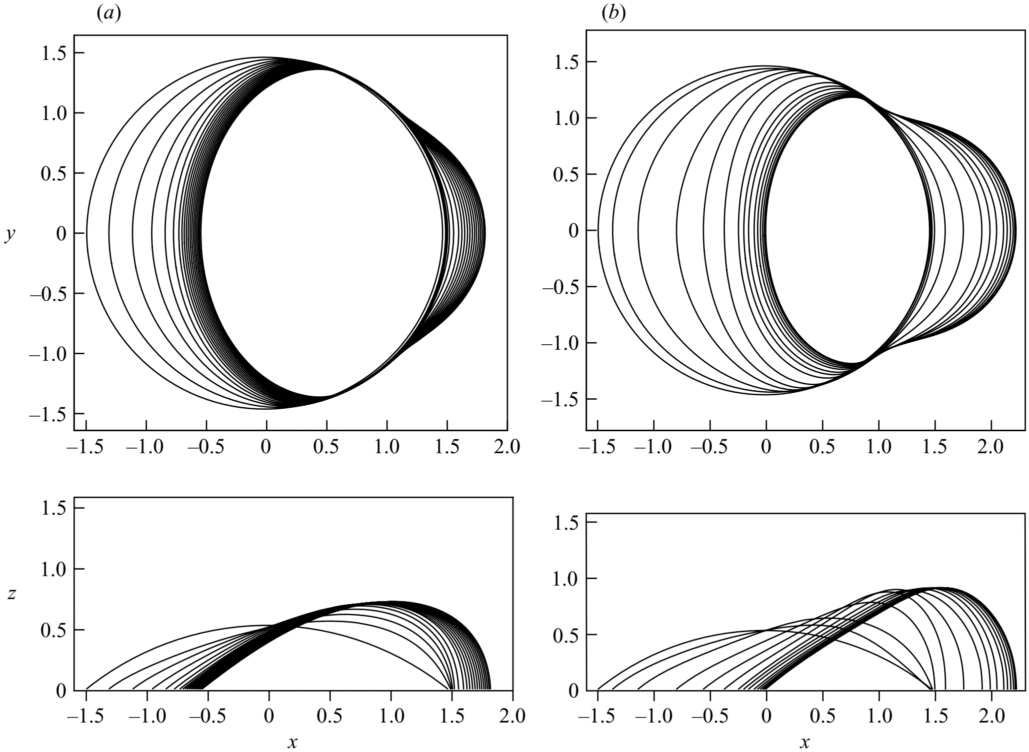

FIGURE 5. Snapshots of the droplet at a time interval of 2 for Case A at criticality. (*a*) $Re = 0.684$ and $We_c = 0.087$; (*b*) $Re = 74.1$ and $We_c = 3.54$. Contact lines (upper), cross-section (lower).

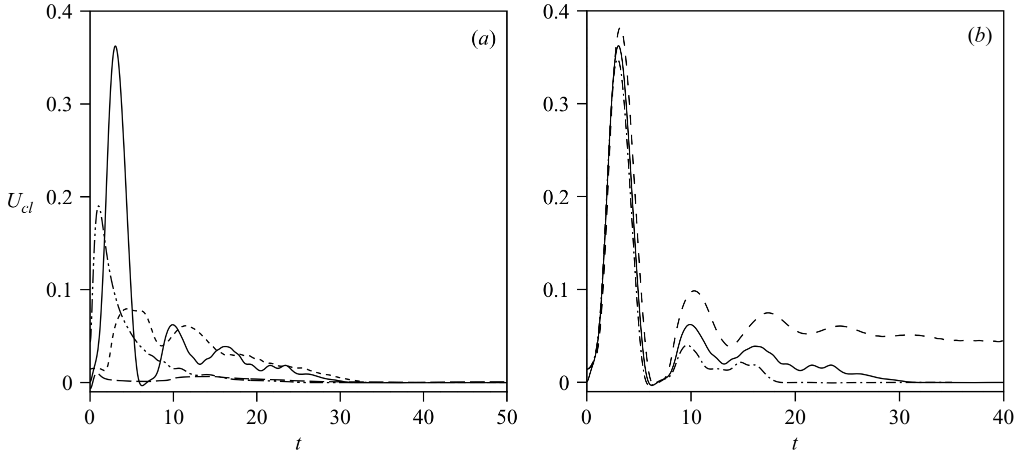

FIGURE 6. Contact line speed as a function of time with $\theta_0 = 90°$, $\theta_A = 90°$ and $\theta_R = 40°$ for Case C. (*a*) Long-dashed and dash-dot-dotted lines denote the contact-line speed at $Re = 0.684$ and $We_c = 0.067$ at the upstream and downstream ends of the contact line; dashed and solid lines denote the contact-line speed at $Re = 74.1$ and $We_c = 3.01$ at the upstream and downstream ends of the contact line, respectively. (*b*) Contact-line speed at the downstream end of the contact line at $Re = 74.1$; dash-dotted, solid and dashed lines denote the results at $We = 2.75$, 3.01 and 3.18, respectively.

the relation between this angle and the instantaneous velocity oscillates, in a similar manner as found in our previous work (Ding & Spelt 2007*a*) on inertial effects in droplet spreading.

The contact-line speed U_{cl} at the upstream and downstream ends of the contact line is plotted as a function of time in figure 6(*a*). U_{cl} was obtained by determining the contact-line position from C using linear interpolation, and subsequently differentiating the position numerically with time. The accuracy of the results displayed in figure 6 is therefore not representative of that of the simulations themselves. (Also, U_{cl} may be affected at very short times by the relaxation of the diffuse interface arising from the initial condition used for C; since the exact distribution of C corresponding to a sphere at equilibrium is not known, we have used an approximation valid as long as the interfacial thickness is much smaller than the drop radius.) Nevertheless it is of interest to note that at $Re = 0.684$, U_{cl} at the downstream end of the contact line decreases to zero monotonically after an initial acceleration, whereas at $Re = 74.1$, both contact line speeds shown are oscillatorily damped to zero in an approximately antiphase manner. It is seen that at a brief instant in the latter case the downstream contact line even moves slightly upstream. In the light of the work by Thiele & Knobloch (2006), it is important to point out though that the cases in figure 6(*a*) are at criticality, and that clearly the oscillations are still damped. Beyond criticality, this is still the case (albeit that the initial amplitude of the oscillations is larger), as can be seen in figure 6(*b*), i.e. the droplet merely reaches a new quasi-steady state (moving at constant speed) in a damped-oscillatory manner. Overall, the oscillatory behaviour is reminescent of that reported in Ding & Spelt (2007*a*) for inertial effects in droplet spreading. We aim to investigate the motion and breakup of three-dimensional droplets on a wall in shear flow in future work.

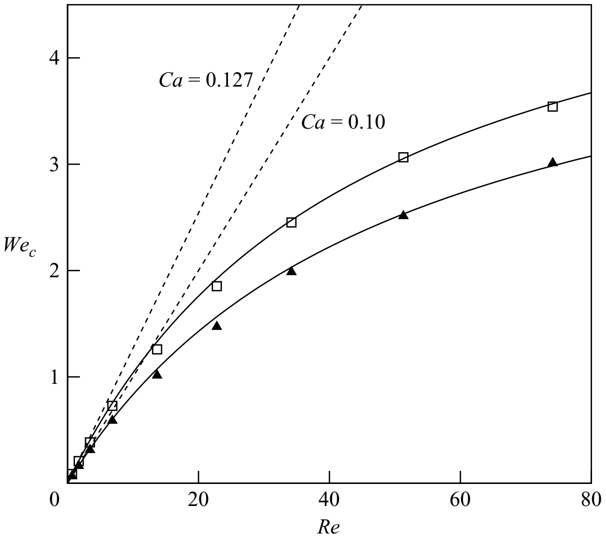

FIGURE 7. Critical Weber number as a function of Reynolds number. Open squares denote the results for Case A and filled triangles for Case C. Solid lines represent the respective curve fits using the approximate relation (3.1): $\alpha = 0.127$ and $\beta = 0.022$ (upper), $\alpha = 0.10$ and $\beta = 0.020$ (lower). Dashed lines represent the slopes ($Ca = We/Re$) obtained in the regime of creeping flows ($Re = 0.684$): $Ca = 0.127$ for Case A and $Ca = 0.10$ for Case C.

3.3. *Critical conditions*

In figure 7 the critical value of the Weber number, We_c, is shown as a function of Re for Cases A and C for density- and viscosity-matched fluids. The slope of the result for Case A at low Re has already been compared in table 1 with the corresponding result by Dimitrakopoulos & Higdon (1998), there being none available for Case C in that work. When Re is increased, We_c deviates from the low-Re result and appears to eventually approach a constant value. This trend is similar to those in the results for two-dimensional droplets (Spelt 2006). We shall follow here the approach in that paper and in earlier work (e.g. Dussan V. 1987; Durbin 1988; Dimitrakopoulos & Higdon 1998; Hodges & Jensen 2002) of adopting a force balance in the streamwise direction to represent this trend. This balance contains a viscous component (tentatively written here as $\alpha_v \mu \dot{\gamma} a^2$) and an inertial component (approximated here by $\alpha_i \rho \dot{\gamma}^2 a^4$) of the force exerted by the outer fluid, and the contribution from the solid substrate arising from contact angle hysteresis ($\approx \alpha_s \sigma(\cos\theta_R - \cos\theta_A)a$), where α_v, α_i and α_s are parameters related to the geometrical shape of the droplet. A further contribution from the wall shear stress inside the drop is assumed to be of the same form as that of the viscous part of the stress exerted by the outer fluid (we consider here viscosity-matched fluids). The resulting approximate force balance at critical conditions can then be written as

$$We_c = \alpha Re/(1 + \beta Re) \tag{3.1}$$

(cf. Spelt 2006), where $\alpha = \alpha_s(\cos\theta_R - \cos\theta_A)/\alpha_v$ and $\beta = \alpha_i/\alpha_v$. Naturally, no explicit results are available for the proportionality factors introduced here, these being dependent on the shape of the droplet (an analytical expression for α_v is available from the work of Sugiyama & Sbragaglia (2008) for the case of a hemispherical droplet in a creeping flow). Obviously, α corresponds to the critical value of the

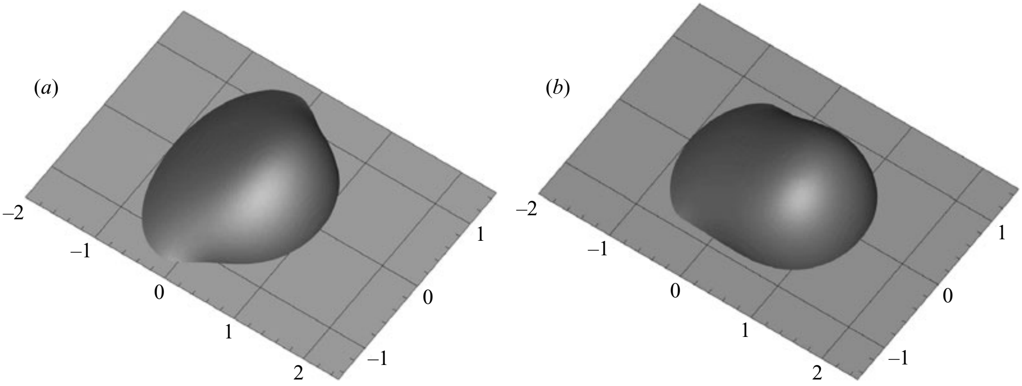

FIGURE 8. Three-dimensional view of the droplet at $Re = 74.1$ at criticality. (a) Case A at $We_c = 3.54$, (b) Case C at $We_c = 3.01$.

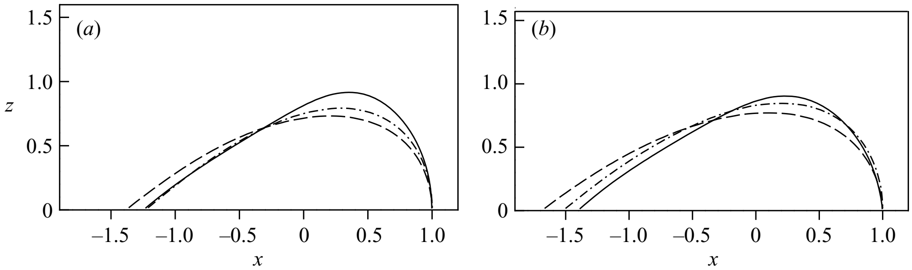

FIGURE 9. Cross-section in the symmetry plane at criticality. Long-dashed line denotes the results at $Re = 0.684$, dash-dotted line for $Re = 6.84$ and solid line for $Re = 74.1$. (a) Case A, (b) Case C. The drops have been shifted such that their downstream ends coincide for clarity.

capillary number at low values of Re, and we have seen above that the results for this parameter compare well with previous work. The solid lines in figure 7 represent curve fits based on (3.1) to the numerical results. It is seen that the results of the numerical simulations are very well represented by this simple expression. For Case A, we found that $\alpha = 0.127$, $\beta = 0.022$; for Case C, $\alpha = 0.10$, $\beta = 0.02$. Regarding the values obtained for β, it is surprising to see that these are virtually identical for the two cases considered. It suggests that even the substantial differences in shape of the drops in the two cases do not have a strong effect on the force balance.

Overall we have found that the shape of drops at criticality does not change (at least not qualitatively) drastically in the range of values of Re considered here. Typical three-dimensional views of the droplet at criticality for moderate Re are shown in figure 8. A quantitative comparison of the cross-section of the droplets for various Re is shown in figure 9. It is seen especially in the latter figure that at larger values of Re, the droplet becomes more erect at criticality. Further inspection of our results for $Re = 74.1$ has shown that the pressure above the top of the drop reaches a distinct minimum, thereby confirming that the drop shape can be associated with the inertial suction effect explained and demonstrated by Feng & Basaran (1994) for flow past a pinned two-dimensional bubble.

The shape of the contact line of the droplets at criticality for various Re is shown in figure 10. In both cases simulated, an increase in Re leads to a decrease in the length and width of the contact line (and in an increase in the height) of droplets

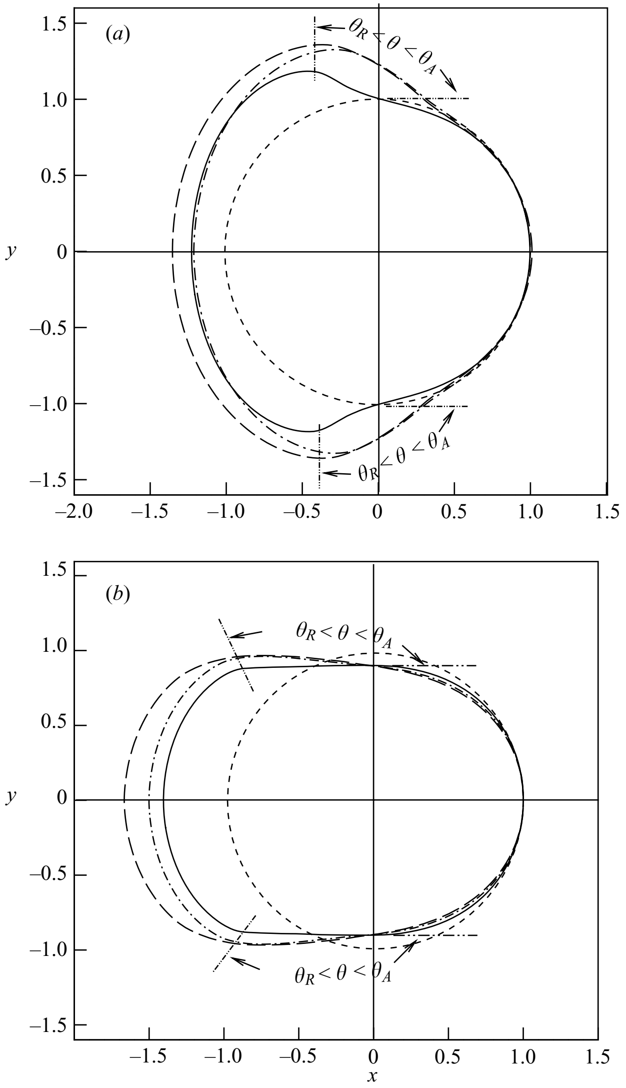

FIGURE 10. Contact line shapes at $Re = 0.684$, 6.84 and 74.1 at criticality. Long-dashed line denotes the results for $Re = 0.684$, dash-dotted line for $Re = 6.84$ and solid line for $Re = 74.1$. Short-dashed line represents the initial circular contact line of Case C as a frame of reference. The part of the contact line where the contact angle changes from θ_R to θ_A is indicated by the intersections of the contact line with the dash-dot-dotted lines. (*a*) Case A, (*b*) Case C. The drops have been shifted such that their downstream ends coincide for clarity.

at criticality. Evidently, this leads to a reduced area wetted by the drop. Because the wetted area may be a concern in heat and mass transfer in practical applications, we present data on this parameter as a function of *Re* in figure 11. Here, the wetted area has been computed by approximating the area of the wall enclosed by the contour $C = 0.5$. The relatively wide droplets in Case A wet a larger area than the long droplets in Case C. The decrease in wetted area when *Re* increases is qualitatively similar, however (close inspection of the data show an approximately exponential decay).

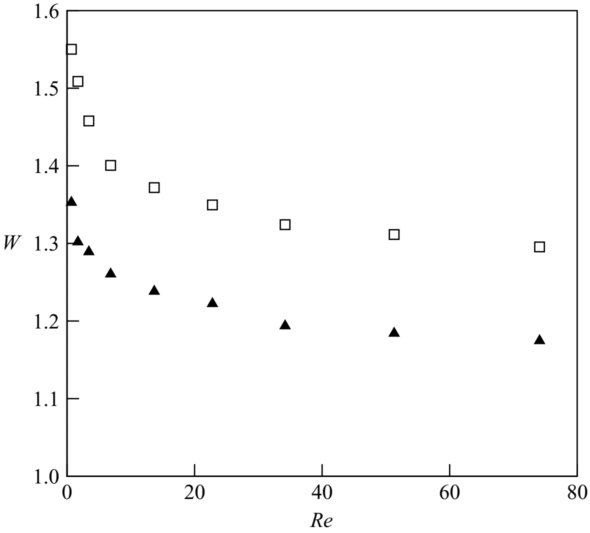

FIGURE 11. Wetted area as a function of Reynolds number at criticality. Open squares denote the results for Case A and filled triangles for Case C. The wetted area has been scaled by πR^2.

It is of interest to note some peculiarities in the shape of the contact line. In Case A, the segment of the contact line wherein $\theta_R < \theta < \theta_A$ (indicated in figure 10) represents the part of the contact line that has not moved at all (see figure 5). A further peculiar feature is that the radius of the local curvature of the downstream portion of the contact line in Case A is close to that of an initial contact line of Case C. In the investigation of contact line shape of a steadily sliding drop on an inclined plate, Dussan V. & Chow (1983) reported that the segments of the contact line on both sides of the drop must be straight lines, along which the contact angle changes from the receding to advancing angle. Though in our cases the drop comes to a halt at criticality, the drop in Case C does approach a shape with parallel sides with circular ends at $Re = 74.1$, whereas this is not observed in Case A. It appears that the transient motion of the contact line has significant effects on the occurrence of the parallel straight sides of the drop. As shown in figures 4 and 5, at criticality, only the contact line of the drop in Case C at $Re = 74.1$ completely departs from its initial position, and slides for a comparatively long distance sufficient for the contact line to adjust to two straight and parallel sides. The transition of the contact angle from θ_R to θ_A starts at the transverse extremity of the contact line and ends at $y \approx 0.9$ for the range of Re studied here (recall the rescaling of the coordinates in the graphs by R).

3.4. *Effect of slip length*

We investigate here the effect of the effective slip length on the contact line shape and contact line speed, and choose Case A at $Re = 6.84$ as the test case. The effective value of the slip length is changed by using different values of the thickness of the diffuse interface, which is prescribed by ϵ. The value of We is set to 0.58, which is slightly above the critical value $We_c = 0.56$, since we expect the effect of the slip length to be more significant than in cases that lead to a stationary drop. A fine mesh $450 \times 150 \times 150$ with $\epsilon = 0.011a$ is used to produce a smaller slip length of $0.022a$, compared to the slip length $\kappa = 0.041a$ in most other simulations in this study. Results are shown in figure 12, in terms of the contact line shape at $t = 20$ and contact line speed versus time. It is seen that, although at an early stage the contact-line motion

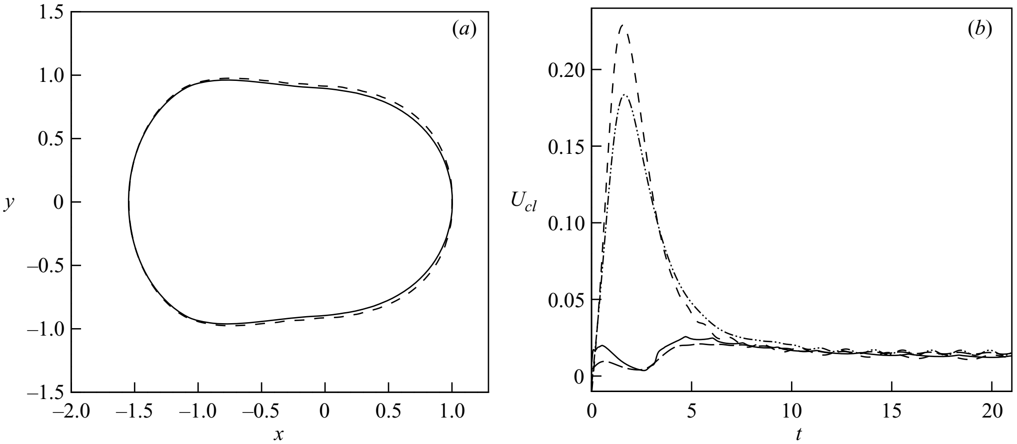

FIGURE 12. Effect of effective slip length κ illustrated by solutions for Case A at $Re = 6.84$ and $We = 0.58$. (*a*) Contact line shapes at $t = 20$, where solid line denotes $\kappa = 0.041a$ and dashed line denotes $\kappa = 0.022a$. (*b*) Contact line speed as a function of time, where long-dashed and dash-dot-dotted lines denote the contact-line speed at $\kappa = 0.041a$ at the upstream and downstream ends of the contact line, respectively, while solid and dashed lines denote the contact-line speed at $\kappa = 0.022a$ at the upstream and downstream ends of the contact line, respectively. In (*a*), the drops have been shifted such that their upstream ends coincide for clarity.

at the downstream side is the largest when the slip length is larger, the drop moves at more or less the same approximately constant speed in both cases at a later stage. Good agreement in contact line shapes is also seen at that stage. We conclude that the magnitude of the slip length for the range of values simulated does not affect the contact line speed significantly when the droplet is in equilibrium, but affects the dynamic behaviour of moving contact line earlier on.

3.5. *Effect of viscosity and density ratio*

We investigate here the effects of varying the viscosity and density ratios, although a full parametric study is not attempted. In the following, we reconsider the simulations for $\lambda_\rho = \lambda_\mu = 1$, $Re = 74.1$, with $We = 3.54$ (Case A) and $We = 3.10$ (Case C), which are close to the respective critical values, and reduce the viscosity or density of the surrounding fluids, keeping the fluid properties of the droplet unchanged. Hence in the following, $Re = 74.1\lambda_\mu/\lambda_\rho$ and $We = \{4.43, 3.10\}/\lambda_\rho$. Four tests with different density and viscosity ratios have been simulated: $\lambda_\rho = 10$, $\lambda_\mu = 1$; $\lambda_\rho = 100$, $\lambda_\mu = 1$; $\lambda_\rho = 1$, $\lambda_\mu = 3$; $\lambda_\rho = 1$, $\lambda_\mu = 10$. We note here that, although the wake of the drop for the case of $\lambda_\rho = 1$, $\lambda_\mu = 10$ (such that $Re = 740$) was unsteady, which could be affected by the fact that only half the drop is simulated, we have included this result for completion. The results for the contact angle distribution are presented in figure 13; the corresponding contact line shapes are shown in figure 14.

It can be seen in figure 13 that in all flows there is less variation in the contact angle along the contact line for cases with a density or viscosity contrast, suggesting increased stability. This is especially true for Case C with $\lambda_\rho > 1$. This trend is consistent with the force balance analysis in § 3.3 and the results shown in figure 7 for $\lambda_\mu = \lambda_\rho = 1$. An increase in λ_μ here corresponds to a proportional increase in *Re* whereas *We* remains unchanged. Since here we compare with results for $\lambda_\mu = 1$ at a relatively large value of *Re*, a further increase in *Re* is expected to result in a small

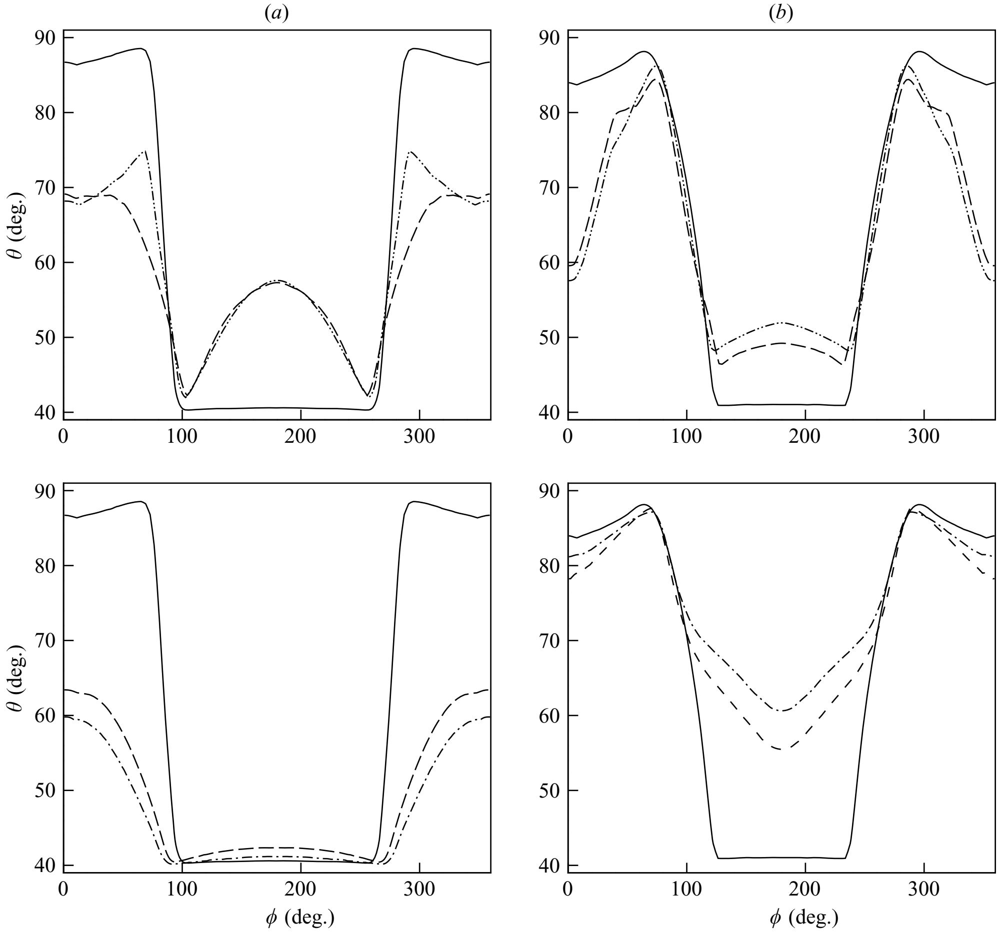

FIGURE 13. Contact angle distribution along the contact line for fluids with viscosity contrast (the upper panels) and density contrast (lower panels) for (*a*) Case A and (*b*) Case C. See figure 2 for the definition of the angle ϕ . Solid line denotes the results for $\lambda_\mu = \lambda_\rho = 1$, long-dashed line for $\lambda_\mu = 10$ and $\lambda_\rho = 1$, dash-dot-dotted line for $\lambda_\mu = 3$ and $\lambda_\rho = 1$, dashed line for $\lambda_\mu = 1$ and $\lambda_\rho = 10$, dash-dotted line for $\lambda_\mu = 1$ and $\lambda_\rho = 100$. The respective values of *Re* and *We* are given in the main text.

increase in the critical value of *We*. Hence we expect the results for $\lambda_\mu > 1$ to be somewhat more stable, but not much. When increasing λ_ρ in the way done here, the Reynolds number and the Weber number are lowered by the same factor. Given that We_c increases with *Re* slower than linearly (figure 7), we would expect this to lead to a significantly more stable flow. This is consistent with the results for $\lambda_\rho > 1$. On the other hand, though they are beyond the scope of this paper, two-phase fluid flows with density and viscosity ratios that are much larger than one, i.e. bubbles in liquids, are expected to display a different regime. From the force-balance point of view, an increase of either λ_μ or λ_ρ tends to destablize the flow.

3.6. *Wake structure*

The structure of the wake is rather different from that observed in uniform or shear flow past a solid sphere (cf. Bagchi & Balachandar 2002). In figures 15 and 16 vector plots are shown in several cross-sectional planes for a typical wake. Since an MAC

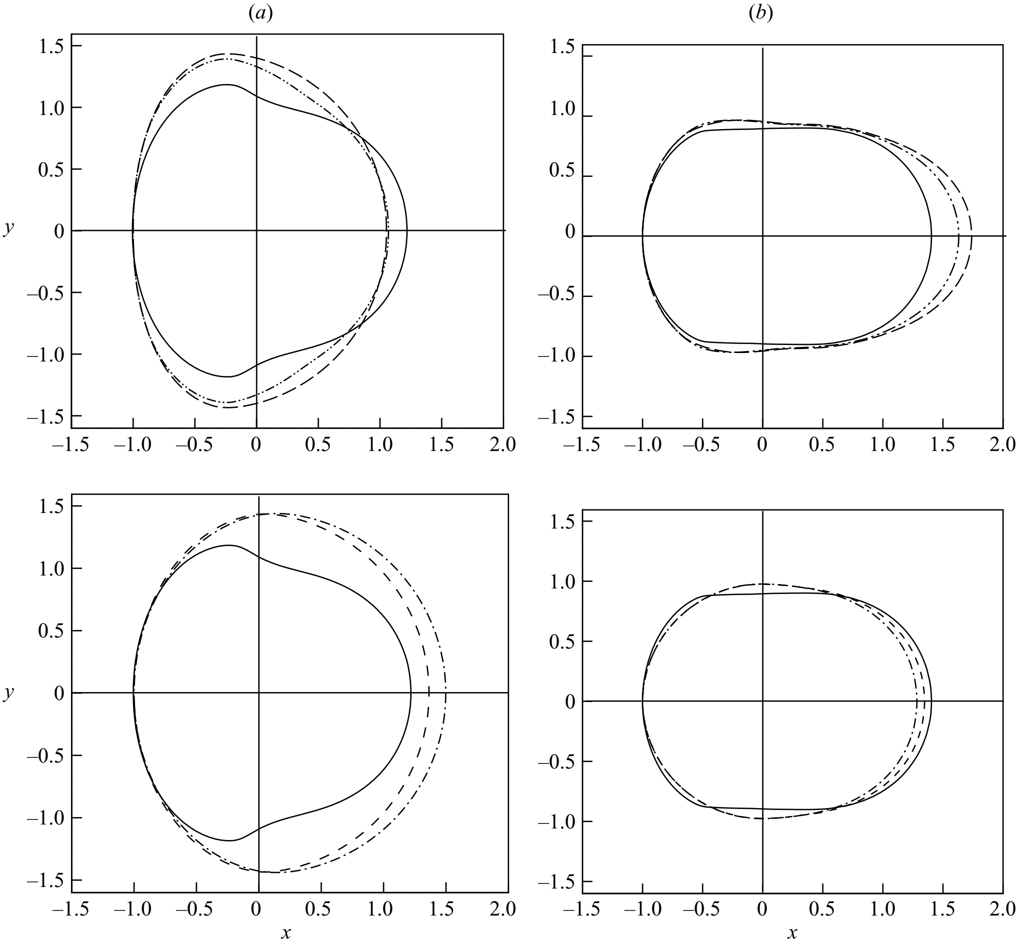

Figure 14. Contact line shapes for fluids with viscosity contrast (the upper panels) and density contrast (lower panels) for (*a*) Case A and (*b*) Case C. Curves as in figure 13. The drops have been shifted such that their upstream ends coincide for clarity.

grid was used in these computations, the various velocity components are computed at different sides of a grid cell; the vectors shown in the figures presented in this section were obtained by averaging at cell centres.

In figure 15(*a*) it is seen that the structure of the wake in the (x, z)-plane resembles that observed previously for the corresponding two-dimensional problem (Spelt 2006), to some extent. The flow inside the drop and that inside a wake circulate in the same direction, such that the wake needs to be separated somewhat from the droplet. The difference with the two-dimensional case in this respect is that there is no full U-turn of the flow in the region between the drop and the wake. As can be seen in figure 15(*b*), fluid particles that just travel narrowly past the top of the droplet come down in the negative z-direction, are then swept sideways in the positive y-direction and subsequently into the x-direction. In the two-dimensional problem, they would move back up in the positive z-direction instead (Spelt 2006). The wake structure is complicated further by the flow in the (y, z)-plane, visualized in figure 16. A circulating flow on the side of the droplet (figure 16*a*) was found to extend further

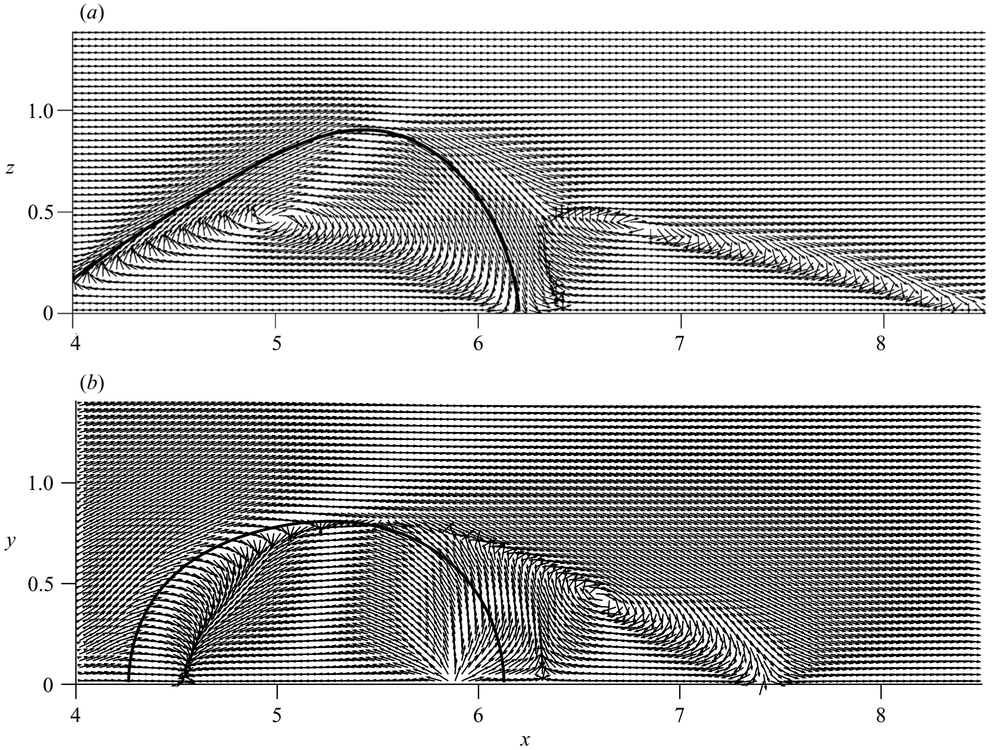

FIGURE 15. Cross-sections showing the structure of the velocity field for Case C at criticality ($Re = 74.1$ and $We = 3.10$), with $\lambda_\mu = \lambda_\rho = 1$. (*a*) (x, z)-plane at $y = 0.0167$; (*b*) (x, y)-plane at $z = 0.3$. The vectors indicate the direction of the velocity in the planes shown and are all of equal length. The vectors are the projections of the three-dimensional velocity vectors on the corresponding two-dimensional planes, and may not be tangential to the droplet surface.

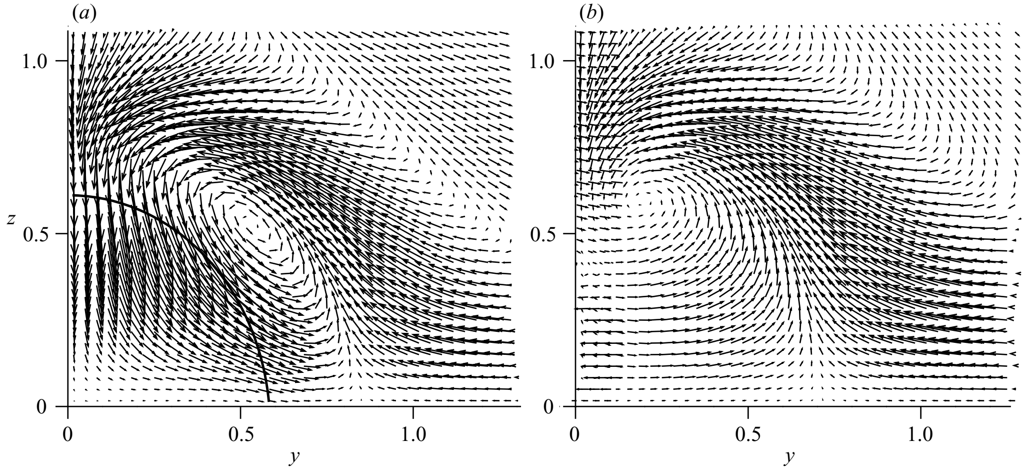

FIGURE 16. Cross-sections showing the structure of the velocity field in the (y, z)-plane for the same case as in figure 15. (*a*) $x = 6$; (*b*) $x = 6.3$. The vectors shown correspond to the projection of the velocity on the (y, z)-plane, and their length is proportional to the magnitude of this projected velocity. The vectors are the projections of the three-dimensional velocity vectors on the corresponding two-dimensional planes, and may not be tangential to the droplet surface.

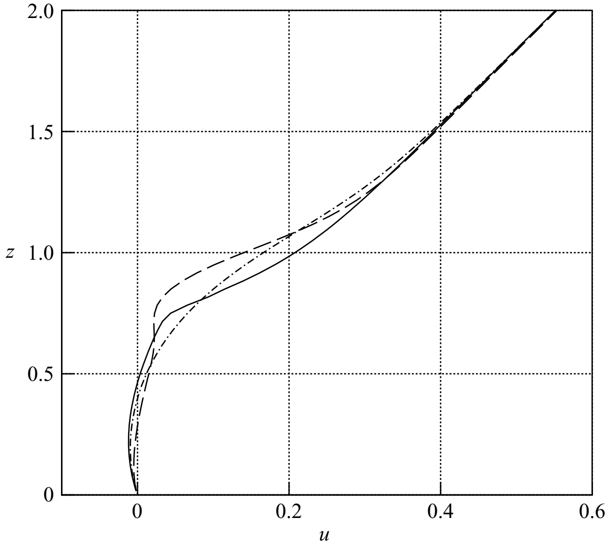

FIGURE 17. Details of profiles of x-component of velocity for $Re = 74.1$ and $We = 3.10$ at criticality for Case C in the same plane as figure 15a , with $\lambda_\mu = \lambda_\rho = 1$. The solid line denotes the profile at $x = 5$, long-dashed line denotes the one at $x = 6$ and dash-dotted line denotes the one at $x = 7$. The velocity has been scaled by the constant speed of the moving upper wall U.

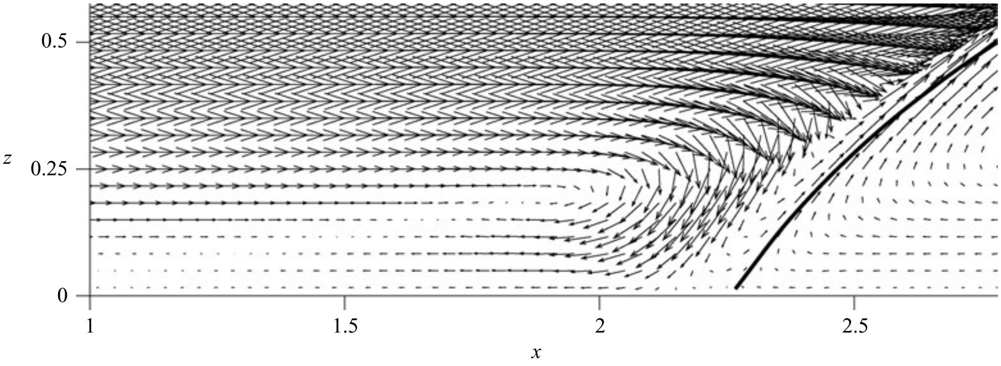

FIGURE 18. Cross-section showing the structure of the velocity field upstream of the droplet in the (x, z)-plane at $y = 0.0167$ for Case C at $Re = 222.3$ with $\lambda_\mu = 3$ and $\lambda_\rho = 1$. The vectors shown correspond to the projection of the velocity on the (x, z)-plane, and their length is proportional to the magnitude of this projected velocity.

downstream inside the wake (figure 16*b*). Profiles of the x-component of velocity are displayed in figure 17 as a function of height. In general, the velocity component varies continuously across the fluid–fluid interface, and its magnitude inside the drop is much smaller than outside. It can also be seen that the magnitude of the x-component velocity does not change with position in the x-direction if $z > 1.5$.

At larger values of the Reynolds number ($Re = 222.3$) an additional structure appeared *upstream* of the droplet. In figure 18 this structure is visualized in an (x, z)-plane close to the symmetry plane. A similar vortex has also been observed by Hwang & Yang (2004) upstream of a wall-mounted cubic obstacle at $Re = 250$ in their numerical investigation of channel flows. The flow is seen to separate at $z = 0.43$. Above this height, the fluid is deflected upwards by the droplet, whereas below it, the fluid is deflected downwards and then is swept sideways in the positive y-direction around the droplet. We note that only a detail of the flow is shown in this figure, and that the thickness of the interface includes the region to the left of the contour $C = 0.5$ wherein the fluid is seen to move upwards even at $z < 0.43$.

4. Conclusions

A diffuse-interface method has been employed to investigate the critical conditions of onset of motion of a three-dimensional droplet in shear flow. The main advantages of the method are that it allows for the contact line to move and for inertial effects. At low *Re*, the contact line shape compares generally well with previous work on creeping flows. At moderate *Re*, inertial effects lead to complicated flow structures around droplets with strong three-dimensional effects, including a highly three-dimensional wake, and, at the largest values of *Re* simulated here, to a structure upstream of the drop. Also, a significant deviation is observed from the critical condition for the onset of motion compared to that predicted by creeping-flow theory. Nevertheless, drops are deformed in a way only modestly different from that in Stokes flows. Furthermore, arguments similar to those employed previously for the two-dimensional problem could be used to represent the critical condition in a straightforward manner.

Further work would be needed to investigate the transition to an unsteady wake, the properties of steadily translating drops, the onset of partial entrainment of drops by the shear flow, as well as experiments beyond the creeping-flow regime.

The authors would like to thank Roman Zhvansky and Ken Mendoza for carrying out preliminary calculations on this problem, and acknowledge financial support from EPSRC under grant nr. EP/D031222.

REFERENCES

Anderson, D. M., McFadden, G. B. & Wheeler, A. A. 1998 Diffuse-interface methods in fluid mechanics. *Annu. Rev. Fluid Mech.* **30**, 139–165.

Bagchi, P. & Balachandar, S. 2002 Shear versus vortex-induced lift force on a rigid sphere at moderate *Re*. *J. Fluid Mech.* **473**, 379–388.

Berejnov, V. & Thorne, R. E. 2007 Effect of transient pinning on stability of drops sitting on an inclined plane. *Phys. Rev.* E **75**, 066308.

Cao, J., Donell, B., Deaver, D. R., Lawrence, M. B. & Dong, C. 1998 In vitro side-view imaging technique and analysis of human t-leukemic cell adhesion to ICAM-1 in *Microvasc. Res.* **55** 124–137.

Dimitrakopoulos, P. 2007 Deformation of a droplet adhering to a solid surface in shear flow: onset of interfacial sliding. *J. Fluid Mech.* **435**, 327–350.

Dimitrakopoulos, P. & Higdon, J. J. L. 1998 On the displacement of three-dimensional fluid droplets from solid surfaces in low-Reynolds-number shear flows. *J. Fluid Mech.* **377**, 189–222.

Dimitrakopoulos, P. & Higdon, J. J. L. 1999 On the gravitational displacement of three-dimensional fluid droplets from inclined solid surfaces in low-Reynolds-number shear flows. *J. Fluid Mech.* **395**, 181–209.

Ding, H. & Spelt, P. D. M. 2007*a* Inertial effects in droplet spreading: a comparison between diffuse interface and level-set simulations *J. Fluid Mech.* **576**, 287–296.

Ding, H. & Spelt, P. D. M. 2007*b* Wetting condition in diffuse interface simulation of contact line motion *Phys. Rev.* E **75**, 046708.

Ding, H., Spelt, P. D. M. & Shu, C. 2007 Diffuse interface model for incompressible two-phase flows with large density ratios *J. Comput. Phys.* **226**, 2078–2095.

Dupont, J.-B., Legendre, D. & Morgante, A. M. 2007 Numerical simulation of static or sliding drop with contact-line hysteresis. In *Proc. 6th Intl Conf. Multiphase Flow, Leipzig, Germany*, paper S4 Wed C37.

Durbin, P. A. 1988 On the wind force needed to dislodge a drop adhered to a surface *J. Fluid Mech.* **196**, 205–222.

Dussan V., E. B. 1987 On the ability of drops to stick to surfaces of solids. Part 3. The influences of the motion of the surrounding fluid on dislodging drops. *J. Fluid Mech.* **174**, 381–397.

Dussan V., E. B. & Chow, R. T. P. 1983 On the ability of drops or bubbles to stick to non-horizontal surfaces of solids. *J. Fluid Mech.* **137**, 1–29.

Feng, J. Q. & Basaran, O. A. 1994 Shear flow over a translationally symmetric cylindrical bubble pinned on a slot in a plane wall. *J. Fluid Mech.* **275**, 351–378.

de Gennes, P. G. 1985 Wetting: Statistics and dynamics. *Rev. Mod. Phys.* **57**, 827–863.

Ha, J. W., Park, I. J. & Lee, S. B. 2005 Hydrophobicity and sliding behavior of liquid droplets on the fluorinated latex films. *Macromolecules* **38**, 736–744.

Hocking, L. M. 1981 Sliding and spreading of thin two-dimensional drops. *Q. J. Mech. Appl. Maths* **24**, 37–55.

Hodges, S. R. & Jensen, O. E. 2002 Spreading and peeling dynamics in a model of cell adhesion. *J. Fluid Mech.* **460**, 381–409.

Hohenberg, P. C. & Halperin, B. I. 1977 Theory of dynamic critical phenomena. *Rev. Mod. Phys.* **49**, 435–479

Hwang, J. Y. & Yang, K. S. 2004 Numerical study of vortical structures around a wall-mounted cubic obstacle in channel flow. *Phys. Fluids* **16**, 2382–2394.

Hyväluoma, J., Koponen, A., Raiskinmäki, P. & Timonen, J. 2007 Droplets on inclined rough surfaces. *Eur. Phys. J.* E **23**, 289–293.

Jacqmin, D. 1999 Calculation of two-phase Navier-Stokes flows using phase-field modelling. *J. Comput. Phys.* **155**, 96–127.

Jacqmin, D. 2000 Contact-line dynamics of a diffuse fluid interface. *J. Fluid Mech.* **402**, 57.

Joanny, J. F. & Robbins, M. O. 1990 Motion of a contact line on a heterogeneous surface. *J. Chem. Phys.* **92**, 3206–3212.

Jones, J. L., Lal, M., Ruddock, J. N. & Spenley, N. A. 1999 Dynamics of a drop at a liquid/solid interface in simple shear fields: A mesoscopic simulation study. *Faraday Discuss.* **112**, 129–142.

Li, X. & Pozrikidis, C. 1996 Shear flow over a liquid drop adhering to a solid surface. *J. Fluid Mech.* **307**, 167–190.

Liu, X. D., Osher, S. & Chan, T. 1994 Weighted essentially non-oscillatory schemes. *J. Comput. Phys.* **115**, 200–212.

Mahé, M., Vignes-Adler, M., Rousseau, A., Jacquin, C. G. & Adler, P. M. 1988 Adhesion of droplets on a solid wall and detachment by a shear flow. *J. Colloid Interface Sci.* **126**, 314–328.

Marsh, J. A., Garoff, S. & Dussan V., E. B. 1993 Dynamic contact angles and hydrodynamics near a moving contact line. *Phys. Rev. Lett.* **70**, 2778–2781.

Nikolayev, V. S. 2005 Dynamics and depinning of the triple contact linein the presence of surface defects. *J. Phys.: Condens. Matt.* **17**, 2111–2117.

Quéré, D., Azzopardi, M. J. & Delattre, L. 1998 Drops at rest on a tilted plane. *Langmuir* **14**, 2213–2216.

Seppecher, P. 1996 Moving contact lines in the Cahn-Hilliard theory. *Intl J. Engng Sci.* **34**, 977–992.

Spelt, P. D. M. 2005 A level-set approach for simulations of flows with multiple moving contact lines with hysteresis. *J. Comput. Phys.* **207**, 389–404.

Spelt, P. D. M. 2006 Shear flow past two-dimensional droplets pinned or moving on an adhering channel wall at moderate Reynolds numbers: a numerical study. *J. Fluid Mech.* **561**, 439–463.

Sugiyama, K. & Sbragaglia, M. 2007 Linear shear flow past a hemispherical droplet adhering to a solid surface. *J. Engng maths* (in press).

Theodorakakos, A., Ous, T., Gavaises, M., Nouri, J. M., Nikolopoulos, N. & Yanagihara, H. 2006 Dynamics of water droplets detached from porous surfaces of relevance to PEM fuel cell. *J. Colloid Interface Sci.* **300**, 673–687.

Thiele, U. & Knobloch, E. 2006 On the depinning of a driven drop on a heterogeneous substrate. *New J. Phys.* **8**, 1–37.

Thoreau, V., Malki, B., Berthome, G., Boulange-Petermann, L. & Joud, J. C. 2006 Physico-chemical and dynamic study of oil-drop removal from bare and coated stainless-steel surfaces. *J. Adhesion Sci. Technol.* **20**, 1819–1831.

Zhang, J., Miksis, M. J. & Bankoff, S. G. 2006 Nonlinear dynamics of a two-dimensional viscous drop under shear flow. *Phys. Fluids* **18**, 072106.